

Article

Effective Removal of Humic Acid by Zr-MOFs with Surface Modification

Yuankang Jiang, Zhenggang Wang, Zhiping Zhu *, Mingpeng He and Pan Zhou

School of Chemistry and Chemical Engineering, Changsha University of Science and Technology, Changsha 410114, China; 17336671180@163.com (Y.J.); zhenggangwang16@163.com (Z.W.); h18707488613@163.com (M.H.); 19109021166@stu.csust.edu.cn (P.Z.)

* Correspondence: zhuzp@csust.edu.cn

Abstract: Humic acid (HA) in makeup water is one of the important safety issues of high-parameter power plants. Herein, the Zr-based metal organic frameworks (Zr-MOFs) were applied to remove humic acid in water. The mesoporous and active sites of Zr-MOFs were controlled by different ratios of ligands to increase the adsorption of HA. The maximum adsorption capacity was 150.15 mg g⁻¹. The morphology and adsorption properties of the Zr-MOFs were characterized using scanning electron microscopy (SEM), X-ray diffraction (XRD), surface charge, Fourier Transform infrared (FT-IR), N₂ adsorption-desorption and adsorption test. The adsorption process of HA accorded with the pseudo-second-order kinetics, while the adsorption isotherm conformed to the Langmuir model and the adsorption was proved to be a spontaneous and endothermic process. Physical adsorption by the mesoporous materials and the hydrogen bonding interactions between the Zr-MOFs and HA were the driving forces of HA adsorption. These results provided useful information for the effective removal of HA and enhanced our understanding of the adsorption mechanism of HA on Zr-MOFs.

Keywords: Zr-MOFs; humic acid; mesoporous; hydrogen bonding; high adsorption capacity



Citation: Jiang, Y.; Wang, Z.; Zhu, Z.; He, M.; Zhou, P. Effective Removal of Humic Acid by Zr-MOFs with Surface Modification. *Water* **2022**, *14*, 1800. <https://doi.org/10.3390/w14111800>

Academic Editors: Weihua Zhao, Kai Wang and Shanyun Wang

Received: 27 April 2022

Accepted: 25 May 2022

Published: 2 June 2022

Publisher's Note: MDPI stays neutral with regard to jurisdictional claims in published maps and institutional affiliations.



Copyright: © 2022 by the authors. Licensee MDPI, Basel, Switzerland. This article is an open access article distributed under the terms and conditions of the Creative Commons Attribution (CC BY) license (<https://creativecommons.org/licenses/by/4.0/>).

1. Introduction

Humic acid (HA) is a kind of supramolecular association of self-assembling heterogeneous and relatively small molecules, which breakdown from the biomass, existing generally in natural water [1]. They are critical hazards when using water, such as the drinking water supply systems and power systems. They could enrich heavy metal or lead to biological instability. Furthermore, HA causes color and taste problems, and can produce disinfection by-products (DBPs), such as trihalomethanes (THMs) and haloacetic acids (HAA) in the drinking water supply system, and with chlorine containing the risk of a carcinogenesis. In power systems, the existence of HA in the makeup water of the power plant may gradually aggregate to the filter surface and cause the water flux of the membranes to rapidly reduce [2,3]. They also inactivate the resin of the ion exchange system [4]. In addition, HA decomposes in a high-temperature and high-pressure environment, and the produced acidic substances cause corrosion on the inner wall of the pipeline in the circulating water system, which affects the safe operation of the power plant [5]. Therefore, it is important to remove HA from drinking and other processed water. At present, different chemical and physical treatments were studied to remove HA, including ion exchange [6], membrane treatment [7], the coagulation sedimentation method [8,9], the oxidation method [10] and photocatalytic degradation [11]. However, these methods still have limitations, such as low removal efficiency. Thus, the question of how to attain high removal efficiency of HA needs further investigation. Adsorption is regarded as one of the most promising methods for removing HA, due to its high efficiency, simplicity and through it being easy to recover and operate [12,13]. Up to now, there many adsorption materials were studied for use in HA removal, such as carbon nanotubes [14], activated

carbon [15], graphene [16], resin [17], bentonite [18], kaolin [19], zeolite [20], iron oxide [21], alumina [22] and MOFs [23,24].

Metal-organic frameworks (MOFs) are highly ordered organic–inorganic hybrid materials, formed by the coordination of metal ions and organic ligands [25]. MOFs have the characteristics of a flexibly adjustable pore structure, large porosity and a large specific surface area [26]. Among numerous MOFs, Zr-MOFs show excellent characteristics, such as water, acid, and alkali resistance [27]. In a previous paper, the average size of the HA is 1.6–2 nm [28], which can be removed by adsorption through mesoporous and functionalized matrix materials. However, the structure of Zr-MOFs is mainly microporous, and a large quantity of research has proved that micropores cannot provide an effective surface area for macromolecular HA [29]. The adsorption capacity and adsorption rate are two important directions for its improvement. Therefore, this is an idea worthy of consideration, to seek an adsorbent with a large mesoporous and rich specific surface of the functional group [30]. Therefore, Zr-MOFs adjusted to a suitable structure are expected to enhance the adsorption performance. The pore structure of MOFs can be adjusted by the type of ligand [31], changing the synthesis conditions [32], adding surfactant [33] and so on. Among them, adjustment of the ratio of organic ligands to control the pore structure of MOFs is a promising direction of development. There are some pioneer works in this aspect. For example, Wang et al. [34] introduced various auxiliary ligands to construct three novel Zn-MOFs, and the adsorption of cationic organic dyes was related to the pore size and the charged framework. Michael et al. [35] generated nine Zr-MOFs with different ligands, and the addition of hydrochloric acid accelerated the synthesis without changing the crystallinity and porosity. The surface properties are related to the surface morphology and functional groups of MOFs, thus affecting the adsorption efficiency [36,37]. Zr-MOFs (UiO-66 series), with Zr_6 nodes and ligands such as 1,4-benzenedicarboxylic acid (H_2BDC) and 2-amino-1,4-benzenedicarboxylic acid ($H_2BDC-NH_2$), were extensively studied in the literature, due to their unusual firm and steady chemical property [38,39].

This study was proposed to increase the adsorption capacity of Zr-MOFs to HA via adjusting the surface properties of the Zr-MOFs with the adjustment of the ratio of organic ligands. For these purposes, the two main purposes of this research were: (a) systematically characterizing Zr-MOFs, such as crystallinity, functional groups, surface topography, pore size distribution and ζ potential and (b) comprehensive analysis of the adsorption process, including the equilibrium, adsorption kinetics, adsorption isotherms and thermodynamics. The findings provided valuable insights into the interaction mechanisms of Zr-MOFs with organic compounds, providing important information, from the effective removal of HA, to the design of Zr-MOFs as adsorbents.

2. Materials and Methods

2.1. Materials

Materials: zirconium tetrachloride ($ZrCl_4$, 98%, Macleans), terephthalic acid (H_2BDC , 98%, Macleans), 2-aminoterephthalic acid ($H_2BDC-NH_2$, 95%, Macleans), dimethylformamide (DMF, AR, Shanghai test), ethanol absolute (AR, Zhengzhou). The detailed information about the chemical materials is listed in Table S1, Supplementary Materials. This material was not modified or processed further before use in the experiments. Humic acid sodium salt was acquired from Sigma Aldrich, Berlin, Germany. Humic acid sodium salt (750.0 mg) was dissolved in deionized water (1000 mL) under sonication, and the pH of humic acid solution was adjusted to pH 5.5. Then the solutions were filtered with membrane filters (0.45 μm), and preserved at a low temperature around 4 °C.

2.2. Preparation of Zr-MOFs

This scheme was based on the stable MOF material UiO-66. Different ratios of ligands (the ratios of H_2BDC and NH_2-H_2BDC were 1:0, 1:1, 1:2 and 0:1, respectively) were used to adjust the physicochemical properties of UiO-66, marked as UiO-66, NH_2 -UiO-66 (1:1), NH_2 -UiO-66 (1:2) and NH_2 -UiO-66. The specific process is as follows:

Solution A: A total of 5 mmol $ZrCl_4$ was added to 15 mL DMF and dissolved by ultrasonic over 10 min.

Solution B: A total of 5 mmol of terephthalic acid, 5 mmol of terephthalic acid and amino terephthalic acid (1:1 molar ratio), 5 mmol of terephthalic acid and 2-aminoterephthalic acid (1:2 molar ratio) and 5 mmol of 2-aminoterephthalic acid were added to 15 mL DMF, respectively, and then sonicated over 10 min to dissolve.

The solution B was added to solution A and sonicated for 10 min, and the mixed solution was transferred to the 50 mL autoclave liner. The autoclave was placed in an oven at 80 °C for 12 h, and then at 100 °C for 24 h. The obtained product was placed in a 150 mL beaker, washed alternately in DMF and absolute ethanol three times, centrifuged, and the washed product was vacuum dried at 60 °C for 12 h to obtain Zr-MOFs with different ratios of ligands.

2.3. Characterization

A total of 2 mg of the prepared powder was added to a 1 mL centrifuge tube, then 1 mL of anhydrous ethanol was added, and the sample was sonicated for 10 min to disperse it. A 5 mm × 5 mm conductive adhesive was placed on the carrier table with tweezers and a 5 mm × 5 mm silicon wafer was added, a small drop of the sonicated dispersion was placed on the silicon wafer, and it was placed in an oven at 80 °C for 15 min. The dried samples were put into the gold spraying device together with the carrier table and sprayed with gold for 1 min. The morphology was characterized by a German ZEISS-type field emission scanning electron microscope with the voltage setting of 8–12 kV and the ultimate resolution of 1 nm. The 40 mg sample was placed in the center of the flat slot of the sample table, compacted with a hard plate, scraped off the sample above the upper surface, and the sample was cleaned outside the slot. The X-ray diffractometer is equipped with a $CuK\alpha$ source, a software parameter Twin-secondary of 5, a voltage of 40 kV, a current of 40 mA, a step time of 0.2 s, and a test angle range of 5–40°. A Thermo IS 10 FT-IR spectrometer from the USA was used to characterize the functional groups of the material for FT-IR testing. Dried 2 mg of powder specimens and 200 mg of pure KBr were finely ground under tungsten lamp, placed in a mold and pressed into a transparent sheet on a hydraulic press, and the specimens were put into an IR spectrometer for testing in the wave number range 4000–400 cm^{-1} , scan number 32, and resolution 4 cm^{-1} . For the nitrogen adsorption and desorption test, the specific surface area and pore size distribution of the materials were measured using an ASAP2020 fully automated specific surface and pore size analyzer from Mike's USA. A 300 mg sample was dried under vacuum at 120 °C for 6 h to remove the water from the pores. The degassing temperature of the instrument was arranged at 120 °C and the degassing time was 6 h. X-ray photoelectron spectroscopy (XPS) was performed using Omnicron XPS.

2.4. HA Adsorption Test of Zr-MOFs

Here, the 0.1 g sample was weighed into HA solution with the magnetic stirrer on. Samples were taken at 0, 0.5, 1, 2, 5, 10, 20, 50, 100, 200, 300, 400, 600, 800, 1000, 1400 and 1800 min, and the absorbance of the solution was detected at 254 nm with an ultraviolet-visible spectrophotometer. To study the process of the adsorption isotherm models, the adsorption tests of HA on the four different Zr-MOFs were recorded at different concentrations (7.5, 15, 30, 45, 60, 90 $mg L^{-1}$) and different temperatures (15, 25, 35 °C). The results of the removal efficiency of HA were determined by the calibration curve. The following equation was used to calculate the amount of HA adsorbed on the four different Zr-MOFs:

$$Adsorption\ capacity\ (q) = \frac{(c_0 - c_t)v}{m} \quad (1)$$

Use the following formula to calculate HA removal efficiency:

$$Removal\ efficiency\ (R) = \left(\frac{c_0 - c_t}{c_0} \right) \times 100\% \quad (2)$$

Here, q (mg g^{-1}) and R were the adsorption capacity and removal efficiency at equilibrium, respectively. c_0 (mg L^{-1}) and c_t (mg L^{-1}) represented the concentration of HA at time 0 and t h, respectively. m (g) and v (L) were the weight of Zr-MOFs and the volume of humic acid solution.

2.5. Adsorption Kinetics and Isotherms

In order to better comprehend and optimize the adsorption process, the kinetics experiments were investigated using pseudo-first-order, pseudo-second-order models and intra-particle dissemination. These models are described below:

$$\lg(q_e - q_t) = \lg q_e - \frac{k_1 t}{2.303} \quad (3)$$

$$\frac{t}{q_t} = \frac{1}{k_2 q_e} + \frac{t}{q_e} \quad (4)$$

$$q_t = k_{id} t^{1/2} + C_i \quad (5)$$

Here q_t (mg g^{-1}) and q_e (mg g^{-1}) represented the adsorption capacity of HA on Zr-MOFs at adsorption and equilibrium time, respectively. The above rate constants included k_1 , k_2 , and k_i are, respectively, from the quasi-first-order, quasi-second-order and intraparticle diffusion models, as shown in Equations (3)–(5).

The two common models of Langmuir and Freundlich were utilized for calculating the adsorption isotherms, as shown in Equations (6) and (7):

$$\frac{C_e}{q_e} = \frac{C_e}{q_m} + \frac{1}{K_L q_m} \quad (6)$$

$$\ln q_e = \ln K_F + \frac{1}{n} \ln C_e \quad (7)$$

C_e (mg L^{-1}) was the equilibrium concentration of the HA solution; q_e (mg g^{-1}) and q_m (mg g^{-1}) represented, respectively, the equilibrium adsorption capacity and theoretical adsorption capacity; K_L (L mg^{-1}) and K_F ($\text{L}^{1/n} \text{mg}^{-1-1/n} \text{g}^{-1}$) were constant related to Langmuir and Freundlich, respectively. The parameter of heterogeneity was $1/n$.

3. Results

3.1. Morphology and Structure of Zr-MOFs

For identification of the synthesized Zr-MOFs, XRD analysis was performed, and the results are shown in Figure 1. Sharp peaks could be observed in the XRD pattern of synthesized Zr-MOFs, which showed they were highly crystalline. The main peaks at $2\theta = 7.6^\circ$, 8.7° , 12.2° , 17.3° , 22.5° , 25.6° and 31.4° were, respectively, assigned to (001), (002), (022), (004), (115), (224) and (046) crystal planes, which were consistent with the characteristic diffraction pattern of UiO-66. In this figure, the signal peaks of the four different Zr-MOFs showed no significant difference, which indicated that the phase of UiO-66 remained unchanged. However, the diffraction peak positions of NH_2 -UiO-66 (1:1) and NH_2 -UiO-66 (1:2) were slightly shifted to higher angles in the XRD pattern, which may be caused by the competition of different ligands.

The FT-IR spectra of the obtained materials were used to characterize the functional groups. The spectra of UiO-66, NH_2 -UiO-66 (1:1), NH_2 -UiO-66 (1:2) and NH_2 -UiO-66 are shown in Figure 2. The sharp peaks at 1658 cm^{-1} and 1384 cm^{-1} were attributed to the stretching of C=O and C=C of Zr-MOFs [40]. Similarly, the peak at 1259 cm^{-1} is due to the carboxylate (-COOH) of the organic linker in the Zr-MOFs. The peak at 3487 cm^{-1} was assigned to the symmetric stretching of the -NH₂ bond in the aminoterephthalic acid linker, and 656 cm^{-1} corresponds to the carbon-carbon double bond of the benzene ring. These signals listed above, through the chemical structure of the Zr-MOFs, indicated that the Zr-MOFs have an abundance of active sites. The FT-IR spectra of UiO-66,

NH₂-UiO-66 (1:1), NH₂-UiO-66 (1:2) and NH₂-UiO-66 were consistent with the previously reported spectra [41,42]. The N contents of UiO-66, NH₂-UiO-66 (1:1), NH₂-UiO-66 (1:2) and NH₂-UiO-66 were found to be 1.68%, 5.46%, 6.62% and 8.23% of N by XPS, respectively. As the proportion of H₂BDC-NH₂ increased, the N elements carried on the ligand increase. The N in UiO-66 probably originated from the organic solvent DMF, that was immersed inside the material during the washing process.

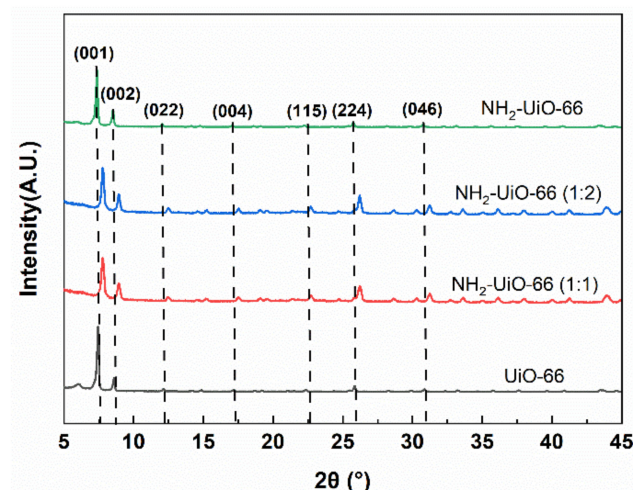


Figure 1. XRD spectra of the four different Zr-MOFs.

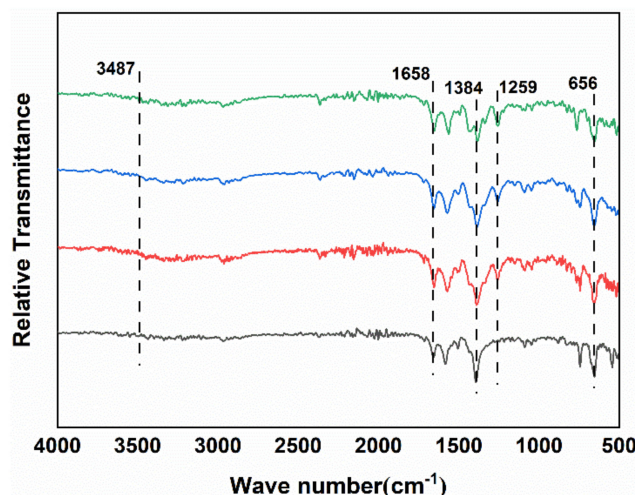


Figure 2. FT-IR spectra of UiO-66, NH₂-UiO-66 (1:1), NH₂-UiO-66 (1:2) and NH₂-UiO-66.

The morphology of four different Zr-MOFs at different ligand ratios were observed through SEM. Figure 3a,b show the original UiO-66, showing a rough granular surface. Figure 3d,f were the SEM images of UiO-66-NH₂ (1:1) and UiO-66-NH₂ (1:2), which, synthesized with the addition of H₂BDC-NH₂, show a more obvious angular shape and uniform ortho-octahedral morphology. The results indicated that the addition of H₂BDC-NH₂ produced better morphology. The average sizes of the four different Zr-MOFs were 90.87 nm, 68.63, 68.41 and 68.16 nm, respectively (Figure 4). The presence of H₂BDC-NH₂ resulted in smaller particle sizes, independent of the amount added. The morphology of the crystalline particles formed was consistent with previous work, which is in agreement with the XRD results.

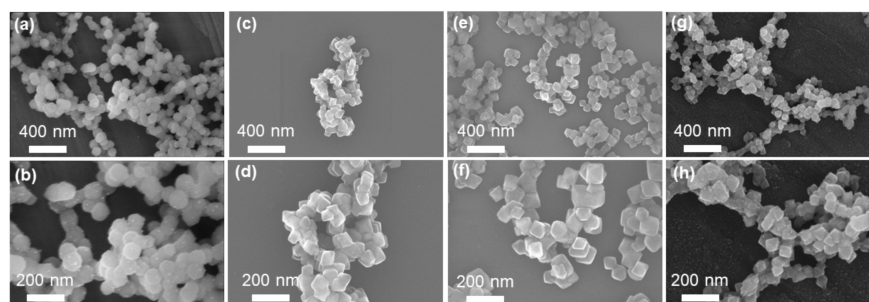


Figure 3. SEM images of UiO-66 (a,b); NH₂-UiO-66 (1:1) (c,d); NH₂-UiO-66 (1:2) (e,f); and NH₂-UiO-66 (g,h).

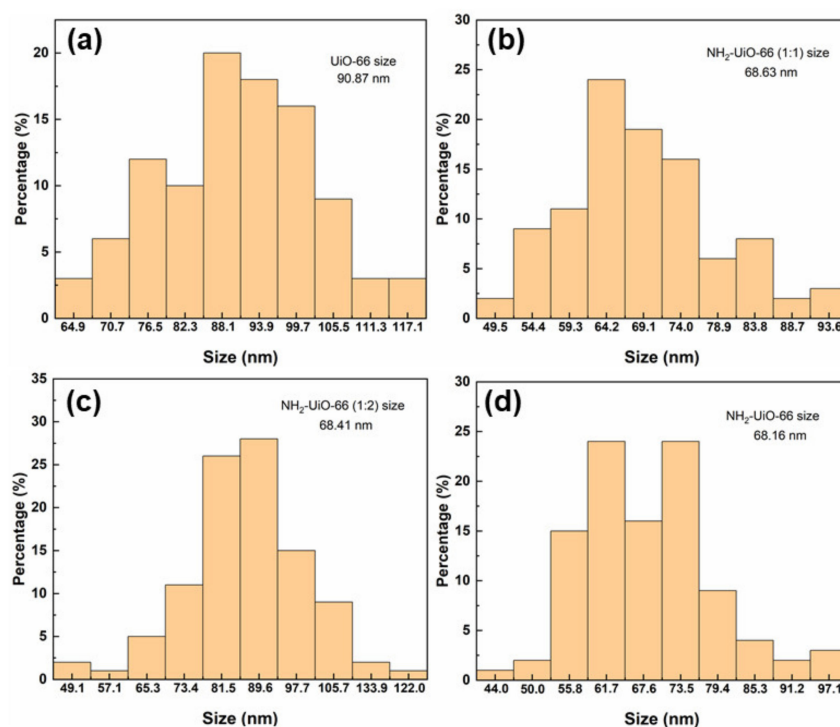


Figure 4. Size distribution of UiO-66 (a); NH₂-UiO-66 (1:1) (b); NH₂-UiO-66 (1:2) (c) and NH₂-UiO-66 (d) counted from SEM images.

The N₂ adsorption–desorption isotherms and pore size distribution of the four different Zr-MOFs are shown in Figure 5. The isotherm of the four different Zr-MOFs exhibited a typical type IV adsorption isotherm. There was a hysteresis loop in the high relative pressure area, which reflected the mesoporous in Zr-MOFs. With the increase in the H₂BDC-NH₂, the pore-size of Zr-MOFs increased after the addition of H₂BDC-NH₂. The Brunauer–Emmett–Teller (BET) surface area also increased with the increase in H₂BDC-NH₂. The BET surface areas of UiO-66, NH₂-UiO-66 (1:1), NH₂-UiO-66 (1:2) and NH₂-UiO-66 were 498.9, 559.3, 625.5 and 277.1 m² g^{−1}, respectively. This result could be assigned to the increase in microporous and mesoporous with the addition of H₂BDC-NH₂. The relatively low surface area of NH₂-UiO-66 may be due to its fewer micropores. After increasing the ratio of H₂BDC-NH₂, the pore volume of mesopores around 3–10 nm gradually increased. It indicated that the number of mesopores was gradually increasing with addition of H₂BDC-NH₂. The increase in the pore volume and specific surface area in the mesopore range may be beneficial to the adsorption of HA.

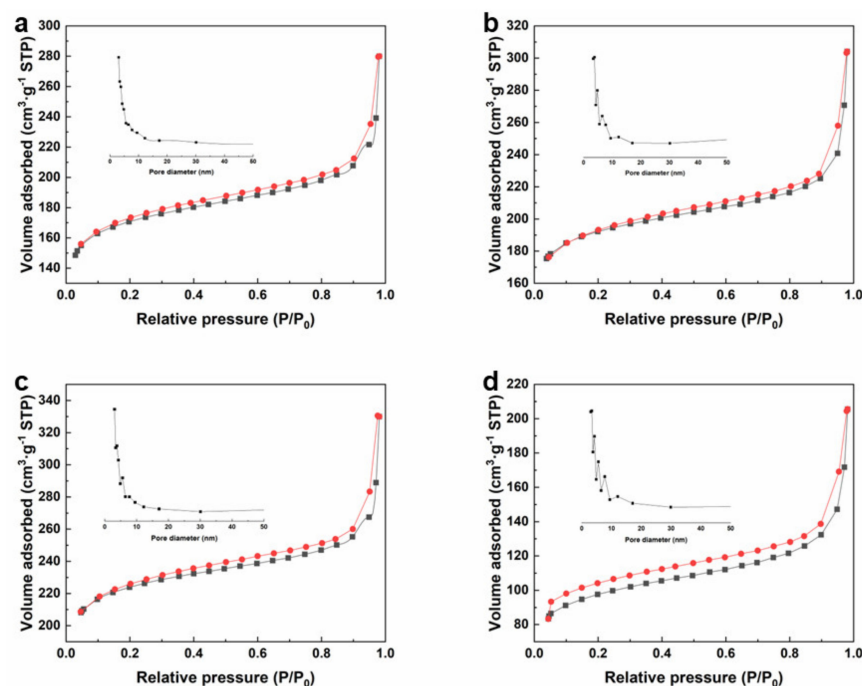


Figure 5. N_2 adsorption-desorption isotherms and pore size distribution of UiO-66 (a); NH_2 -UiO-66 (1:1) (b); NH_2 -UiO-66 (1:2) (c) and NH_2 -UiO-66 (d).

At pH 5.5, the Zeta potentials of UiO-66, NH_2 -UiO-66 (1:1), NH_2 -UiO-66 (1:2) and NH_2 -UiO-66 were tested to be 13.81 mV, 22.20 mV, 27.09 mV and 31.91 mV, respectively. It was easily seen that, as the $H_2BDC-NH_2$ ratio increases, the Zeta potential keeps increasing. This was because the amino group of $H_2BDC-NH_2$ was introduced into the Zr-MOFs as an organic ligand. The Zeta potential of HA, listed in Table S2, Supplementary Materials, was negative at pH 2–11. The Zeta potential of the initial HA solution was tested at -41.64 mV, and the potential value of Zr-MOFs remained positive. This will facilitate the formation of electrostatic interactions to promote the adsorption of the negatively charged HA.

3.2. Kinetics Studies

HA was difficult to remove because of its high solubility and stability in water. However, it is important to improve HA removal due to the public hazard. In terms of the adsorption performance of Zr-MOFs on HA, the adsorption kinetics of Zr-MOFs on HA was studied, and are shown in Figure 6. The adsorption of HA at $25^\circ C$ and pH 5.5 increased fast for the first 0.5 h and then gradually reached equilibrium after 10 h. The removal efficiencies were 34.3%, 55.6%, 65.1% and 85.2% for UiO-66, NH_2 -UiO-66 (1:1), NH_2 -UiO-66 (1:2) and NH_2 -UiO-66, respectively. The results exhibited that NH_2 -UiO-66 could adsorb HA rapidly with high HA removal efficiency. This change may be significantly influenced by the pore size distribution and active functional groups. With the improved effect of the ratio of $H_2BDC-NH_2$, the $-NH_2$ on the surface of Zr-MOFs increased. It was also in line with the increase in the mesopore and the number of functional groups. The q_e increased with the ratio of NH_2-H_2BDC , which was consistent with the mesoporous and number of functional groups' results. These revealed that the surface properties control the Zr-MOFs. For understanding the time dependence of HA removal by Zr-MOFs, kinetic models of the pseudo-first, pseudo-second and intraparticle diffusion were utilized to fit the experimental data. Figure 5b,c showed the results of the adsorption kinetics fitted by pseudo-first-order model and pseudo-second-order model. The correlation coefficients (R^2) of the pseudo-second-order models are 0.991–0.999 (Table 1), which were higher than that of pseudo-first-order model (0.542–0.968). Therefore, the adsorption kinetics of Zr-MOFs on HA could be better described by a pseudo-second-order kinetic model. In order to

investigate the adsorption of different stages of HA removed by four different Zr-MOFs, the fitting curves of the intraparticle diffusion model, which was evaluated for the adsorption process, are shown in Figure 6d. It did not pass through the origin, indicating that intraparticle diffusion was not the only speed-limiting step. The HA diffusion rates of the initial sharp stage (k_{i1}) at first 1 h (Table 2), which was assigned so that the HA migrated from the water to the active sites on the surface of the MOFs. The second stage (k_{i2}) represents the pore diffusion, where the diffusion rate of the $\text{NH}_2\text{-UiO-66}$ was higher than UiO-66. This showed that $\text{NH}_2\text{-UiO-66}$ has more available pores and less steric hindrance. The last stage was the equilibrium stage. The HA adsorbed to $\text{NH}_2\text{-UiO-66}$ would be dispersed into the water and gradually reach a dynamic equilibrium of HA in adsorbent and dissolved in water. After equilibrium, the internal diffusion was no longer a rate-controlling step.

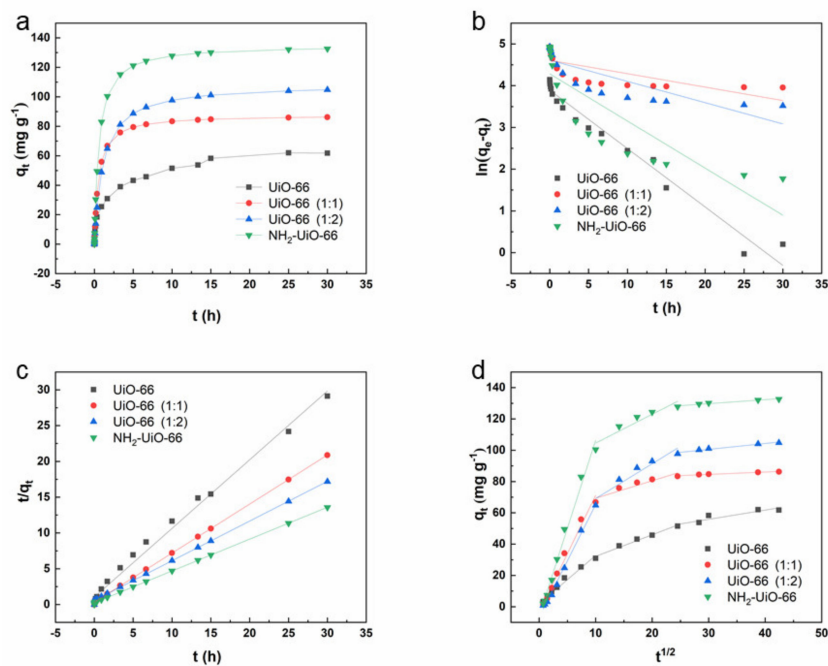


Figure 6. Adsorption kinetic curves (a); adsorption kinetics fitted by pseudo-first-order model (b); pseudo-second-order model (c) and intra-particle diffusion model (d) of HA by four different Zr-MOFs at 25 °C and pH 5.5.

Table 1. Proposed primary and secondary kinetic parameters for the adsorption of HA by Zr-MOFs.

Zr-MOFs	Pseudo-First-Order		Pseudo-Second-Order	
	k_1/min^{-1}	R^2	$k_2/\text{min} \cdot \text{g} \cdot \text{mg}^{-1}$	R^2
UiO-66	1.021×10^{-3}	0.968	2.475×10^{-4}	0.991
UiO-66-NH ₂ (1:1)	2.30×10^{-4}	0.542	6.376×10^{-4}	0.999
UiO-66-NH ₂ (1:2)	3.69×10^{-4}	0.683	1.518×10^{-4}	0.999
UiO-66-NH ₂	8.16×10^{-4}	0.729	2.365×10^{-4}	0.999

Table 2. Fitting parameters of intra-particle diffusion model for Zr-MOFs adsorption of HA.

Zr-MOFs	$k_{i1} (\text{mg g}^{-1} \text{min}^{0.5})$	$k_{i2} (\text{mg g}^{-1} \text{min}^{0.5})$	$k_{i3} (\text{mg g}^{-1} \text{min}^{0.5})$	C_{i1}	C_{i2}	C_{i3}	R_1^2	R_2^2	R_3^2
UiO-66	3.088	1.380	0.589	1.888	18.351	38.150	0.989	0.982	0.934
UiO-66-NH ₂ (1:1)	7.468	1.113	0.151	3.088	58.189	79.958	0.993	0.888	0.978
UiO-66-NH ₂ (1:2)	7.189	2.223	0.376	6.635	46.888	89.219	0.997	0.918	0.980
UiO-66-NH ₂	11.232	1.838	0.225	6.028	86.182	122.03	0.995	0.892	0.978

3.3. Isotherm and Thermodynamics Studies

UiO-66-NH₂ showed excellent adsorption in humic acid solution with a pH of 5.5. Figure 7 showed the adsorption of HA by NH₂-UiO-66 at the different temperatures of 15 °C, 25 °C and 35 °C. As shown in Figure 7a, the adsorption capacity (q_e) increased with the initial concentration increase. The adsorption capacities of NH₂-UiO-66 increased with the increasing adsorption temperature, indicating that increasing the adsorption temperature within a certain range is beneficial to the adsorption. In order to understand the adsorption mechanism of HA by NH₂-UiO-66, the Langmuir and Freundlich models were employed to fit the isotherm parameters, as shown in Figures 6c and 7b. Table 3 summarizes the corresponding parameters of the two adsorption models. It could be observed that the R^2 of NH₂-UiO-66 of Langmuir (0.928–0.989) was higher than that of Freundlich (0.744–0.882). These results indicated that the Langmuir model could better describe the adsorption thermodynamics of NH₂-UiO-66 on HA. The isotherm studies illustrated that HA adsorption on NH₂-UiO-66 could be all relevant to the monolayer physical adsorption processes. Mesoporous adsorption and hydrogen interaction lead to physical adsorption. The maximum adsorption capacity (q_m) for HA were also calculated and shown in Table 3. The q_m of NH₂-UiO-66 was 150.15 mg g⁻¹ at 35 °C calculated from the Langmuir model. Previous work reported that the adsorption capacity of HA on other adsorbents was exhibited at between 33.4 and 97.35 mg g⁻¹. The adsorption capacity of NH₂-UiO-66 was 150.15 mg g⁻¹, which was much higher than these adsorbents.

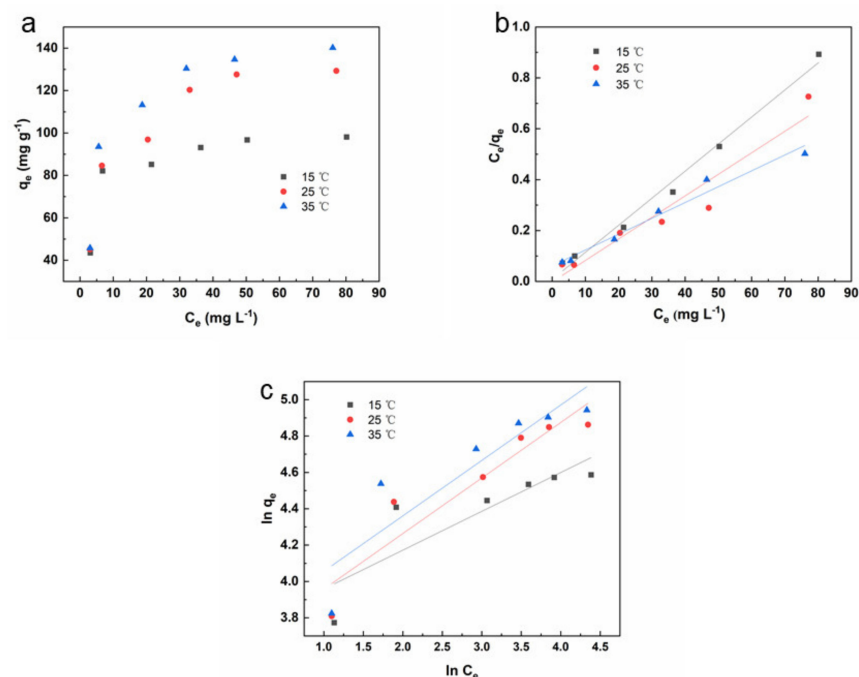


Figure 7. NH₂-UiO-66 adsorption isotherms (a); Langmuir model (b) and Freundlich model fitting results (c) at 15 °C, 25 °C and 35 °C.

Table 3. Langmuir and Freundlich model parameters for adsorption of HA on UiO-66-NH₂.

Model	Parameters	Temperature) (°C)		
		15	25	35
Langmuir	$q_m/\text{mg} \cdot \text{g}^{-1}$	102.15	140.25	150.15
	$K_L/L \cdot \text{mg}^{-1}$	0.302	0.165	0.188
	R^2	0.989	0.928	0.973
Freundlich	$K_F/L^{1/n} \cdot \text{mg}^{-1-1/n} \cdot \text{g}^{-1}$	42.31	38.55	42.56
	R^2	0.744	0.882	0.770

3.4. The Effect of pH on Adsorption

To investigate the effect of pH, the initial pH of the humic acid was adjusted to 2–12 using hydrochloric acid and sodium hydroxide, and the removal efficiencies of humic acid by Zr-MOFs with various ligand ratios were tested. As shown in Figure 8, the removal efficiency of humic acid was significantly higher at lower pH values than at higher pH values. It may be that the carboxyl group binds hydrogen ions at a pH less than 4, and the hydrophobic interaction of the benzene ring and carboxyl group with Zr-MOFs promotes the binding. At pH 4–6, the carboxyl groups start to dissociate, while at a higher pH the phenolic hydroxyl groups start to dissociate and the hydrophobic interactions decrease. At pH 10, the binding mainly relied on the π - π stacking, and when the pH was higher, there was a decomposition of Zr-MOFs, probably due to the hydroxyl radical binding to the carboxyl functional group of Zr-MOFs.

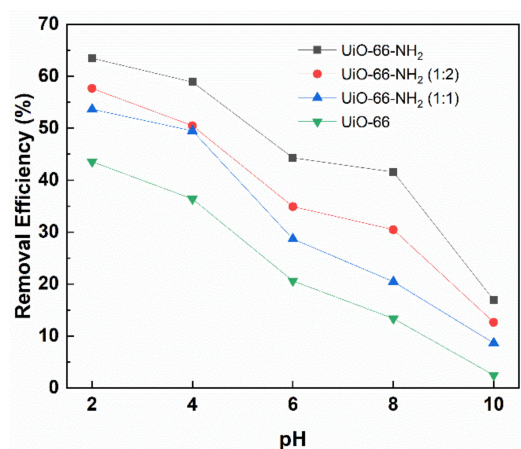


Figure 8. Effect of pH on HA removal by Zr-MOFs.

3.5. The Effect of Salt Concentration on Adsorption

To investigate the effect of salt concentration on the adsorption of HA by Zr-MOFs, humic acid solutions with different concentrations of NaCl were prepared, and the removal efficiencies are shown in Figure 9. The removal efficiency of humic acid by Zr-MOFs were all significantly increased with the increase in ionic strength. It was possible that the ionic strength compressed the thickness of the diffuse double layer on HA, which made the Zr-MOFs more accessible to the HA molecules. An increase in ionic strength also minimized the electrostatic repulsion between ionized oxygen-containing groups, which lead to a reduction in the size of HA molecules and a faster diffusion of coiled HA [43].

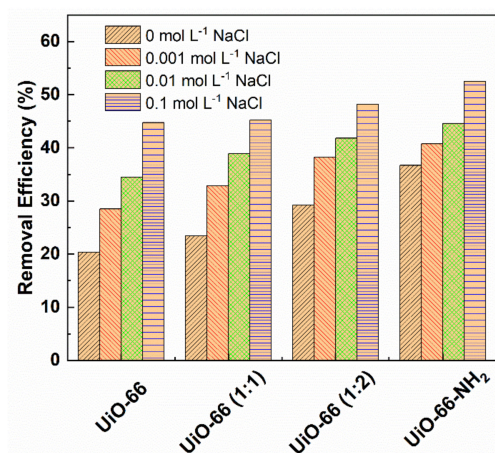


Figure 9. Effect of salt concentration on the removal efficiency of humic acid adsorbed by Zr-MOFs.

3.6. The mechanism of Adsorption

According to the results of the characterization and the experiments, when ligands with amino groups were added, the formed Zr-MOFs tended to show higher surface pore sizes with increasing H₂BDC-NH₂. On the one hand, the amino group in H₂BDC-NH₂ exhibited stronger electrostatic interaction, also facilitating the formation of hydrogen bonding to HA. On the other hand, the increase in the pore size was positively correlated with the adsorption capacity, as shown in Figure 10. Thus, the adsorption capacity of HA was increased through active sites and mesopores.

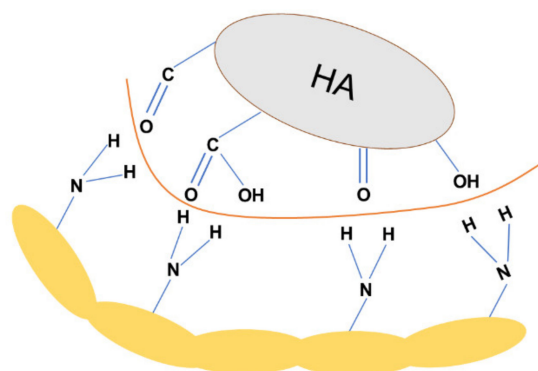


Figure 10. Mechanism diagram of hydrogen bond.

4. Conclusions

The pore size and surface properties of Zr-MOFs were modulated by the addition of two ligands (H₂BDC-NH₂ and H₂BDC) in different ratios (0:1, 1:1, 1:2 and 1:0). The pore size of the mesopores of Zr-MOFs gradually increased, but the crystallinity remained good and the morphology was more regular. NH₂-UiO-66 exhibited excellent HA removal efficiency and the theoretical maximum adsorption capacity could reach 150.15 mg g⁻¹ at pH 5.5. The adsorption process was in accordance with quasi-secondary kinetics and the adsorption isotherms were in accordance with the Langmuir model. The adsorption of HA on Zr-MOFs was found to be driven by the adsorption of mesoporous monolayers on Zr-MOFs. The enhanced effect of humic acid removal from water was due to the increased mesopore size and active sites. With the increase in the number of amino groups and mesopore pore size, the effect of electrostatic interaction and pore size adsorption favors the adsorption of HA. According to this work, the removal of HA in water treatment, by tuning the suitable shape and properties of the ligand-controlled Zr-MOFs, has great potential applications.

Supplementary Materials: The following supporting information can be downloaded at: <https://www.mdpi.com/article/10.3390/w14111800/s1>, Table S1: The applied materials properties, Table S2: Zeta potential of HA in water under different pH. References [44–46] are cited in the supplementary materials.

Author Contributions: Y.J., Z.W., Z.Z., M.H. and P.Z. contributed to the study conception and design. Material preparation, data collection and analysis were performed by P.Z., M.H., Z.W., Z.Z. and Y.J. The first draft of the manuscript was written by Y.J. and all authors commented on previous versions of the manuscript. All authors have read and agreed to the published version of the manuscript.

Funding: This work was supported by Hunan Provincial Science and Technology Plan Key Project (2013GK2016).

Institutional Review Board Statement: The subject does not involve ethical issues.

Informed Consent Statement: Not applicable.

Data Availability Statement: The data sets supporting the results of this article are included within the article and its additional files.

Conflicts of Interest: The authors have no relevant financial or non-financial interests to disclose.

References

1. Piccolo, A. The supramolecular structure of humic substances: A novel understanding of humus chemistry and implications in soil science. In *Advances in Agronomy*; Academic Press: Cambridge, MA, USA, 2002; pp. 57–134.
2. Anjum, T.; Tamime, R.; Khan, A.L. Mixed-Matrix Membranes Comprising of Polysulfone and Porous UiO-66, Zeolite 4A, and Their Combination: Preparation, Removal of Humic Acid, and Antifouling Properties. *Membranes* **2020**, *10*, 393. [[CrossRef](#)] [[PubMed](#)]
3. Lowe, J.; Hossain, M.M. Application of ultrafiltration membranes for removal of humic acid from drinking water. *Desalination* **2008**, *218*, 343–354. [[CrossRef](#)]
4. Levchuk, I.; Marquez, J.J.R.; Sillanpaa, M. Removal of natural organic matter (NOM) from water by ion exchange—A review. *Chemosphere* **2018**, *192*, 90–104. [[CrossRef](#)] [[PubMed](#)]
5. Zhu, Z.P.; Qiao, Y.; Wang, N.N.; Cao, J. Decomposition characteristics of humic acid in boiler make-up water in power plants. *Appl. Therm. Eng.* **2018**, *128*, 1159–1164. [[CrossRef](#)]
6. Mansha, M.; Kazi, I.W.; Manzar, M.S.; Ahmed, T.; Waheed, A.; Ullah, N.; Blaisi, N.I. Ultrahigh removal of methyl orange, acid blue-92 and malachite green by a novel triazine-based polyamine resin: Synthesis, isotherm and kinetic studies. *Int. J. Environ. Anal. Chem.* **2020**, *8*, 1–19. [[CrossRef](#)]
7. Mahmoudi, E.; Ng, L.Y.; Ang, W.L.; Chung, Y.T.; Rohani, R.; Mohammad, A.W. Enhancing Morphology and Separation Performance of Polyamide 6,6 Membranes By Minimal Incorporation of Silver Decorated Graphene Oxide Nanoparticles. *Sci. Rep.* **2019**, *9*, 16. [[CrossRef](#)]
8. Chen, L.; Xu, Y.H.; Sun, Y.J. Combination of Coagulation and Ozone Catalytic Oxidation for Pretreating Coking Wastewater. *Int. J. Environ. Res. Public Health* **2019**, *16*, 1705. [[CrossRef](#)]
9. Ai, Y.J.; Zhao, C.F.; Sun, L.; Wang, X.K.; Liang, L.J. Coagulation mechanisms of humic acid in metal ions solution under different pH conditions: A molecular dynamics simulation. *Sci. Total Environ.* **2020**, *702*, 9. [[CrossRef](#)]
10. Zazouli, M.A.; Roohafzaee, M.; Shahamat, Y.D.; Yousefi, M. Application of magnetic activated carbon as a catalyst in catalytic ozonation process (COP) for removal and mineralization of humic acid from aqueous solution. *Desalin. Water Treat.* **2021**, *220*, 316–328. [[CrossRef](#)]
11. Mohtar, S.S.; Aziz, F.; Nor, A.R.M.; Mohammed, A.M.; Mhamad, S.A.; Jaafar, J.; Yusof, N.; Salleh, W.N.W.; Ismail, A.F.J.J.o.E.C.E. Photocatalytic degradation of humic acid using a novel visible-light active α -Fe₂O₃/NiS₂ composite photocatalyst. *J. Environ. Chem. Eng.* **2021**, *9*, 105682. [[CrossRef](#)]
12. Hosseinzehi, M.; Ehrampoush, M.H.; Tamaddon, F.; Mokhtari, M.; Dalvand, A. Eco-environmental preparation of magnetic activated carbon modified with 3-aminopropyltrimethoxysilane (APTMS) from sawdust waste as a novel efficient adsorbent for humic acid removal: Characterisation, modelling, optimisation and equilibrium studies. *Int. J. Environ. Anal. Chem.* **2021**, *20*, 1–21. [[CrossRef](#)]
13. Llado, J.; Lao-Luque, C.; Sole-Sardans, M.; Montemurro, N.; Perez, S.; Fuente, E.; Ruiz, B. Elimination of persistent anthropogenic pollutants by micro-mesoporous carbon xerogels. Natural organic matter on surface water and textural properties influences. *J. Environ. Chem. Eng.* **2021**, *9*, 11. [[CrossRef](#)]
14. Zhu, Z.P.; Zhou, Y.; Zhou, Q.H. Preparation of polyurethane foam/carbon nanotube composites and adsorption properties for humic acid. *J. Chang. Univ. Ence Technol.* **2009**, *31*, 1293–1303.
15. Summers, R.S.; Roberts, P.V. Activated carbon adsorption of humic substances: II. Size exclusion and electrostatic interactions. *J. Colloid Interface Sci.* **1988**, *122*, 382–397. [[CrossRef](#)]
16. Liu, T.; Graham, N.; Yu, W.Z. Evaluation of a novel composite chitosan-graphene oxide membrane for NOM removal during water treatment. *J. Environ. Chem. Eng.* **2021**, *9*, 10. [[CrossRef](#)]
17. Bazri, M.M.; Barbeau, B.; Mohseni, M. Evaluation of Weak and Strong Basic Anion Exchange Resins for NOM Removal. *J. Environ. Eng.* **2016**, *142*, 8. [[CrossRef](#)]
18. Derakhshani, E.; Naghizadeh, A. Optimization of humic acid removal by adsorption onto bentonite and montmorillonite nanoparticles. *J. Mol. Liq.* **2018**, *259*, 76–81. [[CrossRef](#)]
19. Heikal, G.E. A Comparison between Kaolin, Montmorillonite Fe-Modified Montmorillonite as Candidate of Upflow Column Media Filter for Humic Acid Removal from SSAS. *Pol. J. Environ. Stud.* **2021**, *30*, 2553–2560. [[CrossRef](#)]
20. Wang, L.L.; Dionysiou, D.D.; Lin, J.M.; Huang, Y.X.; Xie, X.L. Removal of humic acid and Cr(VI) from water using ZnO-30N-zeolite. *Chemosphere* **2021**, *279*, 7. [[CrossRef](#)]
21. Tipping, E. The adsorption of aquatic humic substances by iron oxides. *Geochim. Cosmochim. Acta* **1981**, *45*, 191–199. [[CrossRef](#)]
22. Liu, Z.; Ou, T.; Su, M.; Peng, H.; Chen, D. U(VI) sequestration by Al-rich minerals: Mechanism on phase dependence and the influence of natural organic matter. *Chem. Eng. J.* **2021**, *415*, 128858. [[CrossRef](#)]
23. Zhao, X.; Wang, T.; Du, G.; Zheng, M.; Liu, S.; Zhang, Z.; Zhang, Y.; Gao, X.; Gao, Z. Effective Removal of Humic Acid from Aqueous Solution in an Al-Based Metal–Organic Framework. *J. Chem. Eng. Data* **2019**, *64*, 3624–3631. [[CrossRef](#)]
24. Lin, K.-Y.A.; Chang, H.-A. Efficient adsorptive removal of humic acid from water using zeolitic imidazole framework-8 (ZIF-8). *Water Air Soil Pollut.* **2015**, *226*, 1–17.
25. Seo, P.W.; Song, J.Y.; Jhung, S.H. Adsorptive removal of hazardous organics from water with metal-organic frameworks. *Appl. Chem. Eng.* **2016**, *27*, 358–365. [[CrossRef](#)]

26. Lin, R.B.; Xiang, S.; Zhou, W.; Chen, B. Microporous Metal-Organic Framework Materials for Gas Separation. *Chem. Asian J.* **2020**, *6*, 337–363. [[CrossRef](#)]
27. Cao, Y.; Zhang, H.; Song, F.; Huang, T.; Ji, J.; Zhong, Q.; Chu, W.; Xu, Q. UiO-66-NH₂/GO composite: Synthesis, characterization and CO₂ adsorption performance. *Materials* **2018**, *11*, 589. [[CrossRef](#)]
28. Kilduff, J.E.; Karanfil, T. Trichloroethylene adsorption by activated carbon preloaded with humic substances: Effects of solution chemistry. *Water Res.* **2002**, *36*, 1685–1698. [[CrossRef](#)]
29. Lin, J.; Zhan, Y. Adsorption of humic acid from aqueous solution onto unmodified and surfactant-modified chitosan/zeolite composites. *Chem. Eng. J.* **2012**, *200*, 202–213. [[CrossRef](#)]
30. Zheng, Y.F.; Zhang, H.J.; Ge, S.T.; Song, J.B.; Wang, J.K.; Zhang, S.W. Synthesis of Carbon Nanotube Arrays with High Aspect Ratio via Ni-Catalyzed Pyrolysis of Waste Polyethylene. *Nanomaterials* **2018**, *8*, 556. [[CrossRef](#)]
31. Zhang, R.; Song, W.; Wang, M.; Ji, H. Controlling the size of a Zn-MOF through ligand exchange and pore-tailored ZnO assemblies for size-selective gas sensing. *CrystEngComm* **2019**, *21*, 6414–6422. [[CrossRef](#)]
32. McKinstry, C.; Cussen, E.J.; Fletcher, A.J.; Patwardhan, S.V.; Sefcik, J. Effect of Synthesis Conditions on Formation Pathways of Metal Organic Framework (MOF-5) Crystals. *Cryst. Growth Des.* **2013**, *13*, 5481–5486. [[CrossRef](#)]
33. Zhuang, L.; Ge, L.; Liu, H.; Jiang, Z.; Jia, Y.; Li, Z.; Yang, D.; Hocking, R.K.; Li, M.; Zhang, L. A surfactant-free and scalable general strategy for synthesizing ultrathin two-dimensional metal-organic framework nanosheets for the oxygen evolution reaction. *Angew. Chem.* **2019**, *131*, 13699–13706. [[CrossRef](#)]
34. Wang, X.-N.; Li, J.-L.; Zhao, Y.-M.; Pang, J.; Li, B.; Zhang, T.-L.; Zhou, H.-C. Structural tuning of zinc-porphyrin frameworks via auxiliary nitrogen-containing ligands towards selective adsorption of cationic dyes. *Chem. Commun.* **2019**, *55*, 6527–6530. [[CrossRef](#)] [[PubMed](#)]
35. Katz, M.; Brown, Z.; Colón, Y.; Siu, P.; Scheidt, K.A.; Snurr, R.Q.; Hupp, J.T.; Farha, O.K. A Facile Synthesis of UiO-66, UiO-67 and Their Derivatives. *Chem. Commun.* **2013**, *49*, 9449–9451. [[CrossRef](#)]
36. Chen, Y.; Chen, Q.; Zhao, H.; Dang, J.; Jin, R.; Zhao, W.; Li, Y. Wheat straws and corn straws as adsorbents for the removal of Cr (VI) and Cr (III) from aqueous solution: Kinetics, isotherm, and mechanism. *ACS Omega* **2020**, *5*, 6003–6009. [[CrossRef](#)]
37. Karoyo, A.H.; Dehabadi, L.; Alabi, W.; Simonson, C.J.; Wilson, L.D. Hydration and sorption properties of raw and milled flax fibers. *ACS Omega* **2020**, *5*, 6113–6121. [[CrossRef](#)]
38. Moghaddam, F.M.; Jarahiyan, A.; Heidarian Haris, M.; Pourjavadi, A. An advancement in the synthesis of nano Pd@ magnetic amine-Functionalized UiO-66-NH₂ catalyst for cyanation and O-arylation reactions. *Sci. Rep.* **2021**, *11*, 1–17. [[CrossRef](#)]
39. Chen, Z.; Islamoglu, T.; Farha, O.K. Toward base heterogenization: A zirconium metal-organic framework/dendrimer or polymer mixture for rapid hydrolysis of a nerve-agent simulant. *ACS Appl. Nano Mater.* **2019**, *2*, 1005–1008. [[CrossRef](#)]
40. Li, T.-T.; Liu, Y.-M.; Wang, T.; Wu, Y.-L.; He, Y.-L.; Yang, R.; Zheng, S.-R. Regulation of the surface area and surface charge property of MOFs by multivariate strategy: Synthesis, characterization, selective dye adsorption and separation. *Microporous Mesoporous Mater.* **2018**, *272*, 101–108. [[CrossRef](#)]
41. Zhang, X.; Zhang, N.; Gan, C.; Liu, Y.; Chen, L.; Zhang, C.; Fang, Y. Synthesis of In₂S₃/UiO-66 hybrid with enhanced photocatalytic activity towards methyl orange and tetracycline hydrochloride degradation under visible-light irradiation. *Mater. Sci. Semicond. Processing* **2019**, *91*, 212–221. [[CrossRef](#)]
42. Vakili, R.; Xu, S.J.; Al-Janabi, N.; Gorgojo, P.; Holmes, S.M.; Fan, X.L. Microwave-assisted synthesis of zirconium-based metal organic frameworks (MOFs): Optimization and gas adsorption. *Microporous Mesoporous Mater.* **2018**, *260*, 45–53. [[CrossRef](#)]
43. Doulia, D.; Leodopoulos, C.; Gimouhopoulos, K.; Rigas, F. Adsorption of humic acid on acid-activated Greek bentonite. *J. Colloid Interface Sci.* **2009**, *340*, 131–141. [[CrossRef](#)] [[PubMed](#)]
44. Rauthula, M.S.; Srivastava, V.C. Studies on adsorption/desorption of nitrobenzene and humic acid onto/from activated carbon. *Chem. Eng. J.* **2011**, *168*, 35–43.
45. Wang, J.; Bi, L.; Ji, Y.; Ma, H.; Yin, X. Removal of humic acid from aqueous solution by magnetically separable polyaniline: Adsorption behavior and mechanism. *J. Colloid Interface Sci.* **2014**, *430*, 140–146.
46. Wang, J.; Yue, D.; Cui, D.; Zhang, L.; Dong, X. Insights into adsorption of humic substances on graphitic carbon nitride. *Environ. Sci. Technol.* **2021**, *55*, 7910–7919.